


Controlling surface plasmon polariton losses in the visible spectrum by temperature-induced interband transitions

Marat Spector *Department of Mathematics, Achva Academic College, Arugot 7980400, Israel*Stanislav Derevyanko **School of Electrical and Computer Engineering, Ben Gurion University of the Negev, Beer Sheva 84105, Israel* (Received 26 January 2022; revised 21 July 2022; accepted 29 August 2022; published 9 September 2022)

We study theoretically the temperature dynamics at the metal-dielectric interface excited by a strong pump surface plasmon polariton pulse propagating along it. We demonstrate that the inclusion of the interband transitions leads to much stronger temperature-induced modulation of the imaginary part of the dielectric constant induced by the pump. We show that in the visible part of the spectrum a strong pump field can even lead to the decrease in the extinction coefficient for the co- or contrapropagating probe wave.

DOI: [10.1103/PhysRevB.106.125111](https://doi.org/10.1103/PhysRevB.106.125111)

I. INTRODUCTION

Surface plasmon polaritons (SPPs) represent highly localized electromagnetic excitations propagating along a metal-dielectric boundary. High confinement, increased sensitivity to the surface conditions, enhanced electromagnetic field at the interface, and relative flexibility in the engineering implementations make SPPs an attractive tool for applications such as sensing, thin-film solar cells, second-harmonic generation, fluorescence, integrated optical circuits, ultrafast switching, and optical computing, just to name a few [1–4].

However, due to high conductivity of the metallic subsystems the SPPs suffer strong losses and are effectively evanescent wave structures with a longitudinal decay rate of the order of few micrometers in the visible range. It is therefore desirable to find a mechanism that would allow one to control the SPP extinction and manipulate it at picosecond and subpicosecond time scales. This is necessary for ultrafast optical switching and routing applications where plasmonics is used.

In particular, an ultrafast SPP-based optical switch should be able to control the extinction coefficient for a propagating SPP (at a given spectral range) and by transiently reducing the losses make the medium transparent in the longitudinal direction. One way of controlling the electromagnetic properties of the SPP is by use of Bragg resonances in the plasmonic system with artificially created one-dimensional (1D) or 2D periodicity—so-called plasmonic crystals (PCs) [5–9]. Transient plasmonic crystals, where the periodic modulation of the real part of the dielectric function was induced by a spatially periodic pulse, were reported in Ref. [10], while in our previous publication [9] we have studied the periodic 2D plasmonic crystal created by crisscross irradiation of the interface by two plane waves. In particular, in Ref. [9] we have studied the effect of the Bragg resonances on the SPP losses (the imag-

inary part of the dielectric function) and showed that rather than opening a band gap in the band structure of the PC the Bragg resonances caused increased transparency (decreased extinction coefficient) near the resonant frequency.

In this paper, we look at the induced loss modulation from a different angle and study a pump-probe configuration when a weak probe SPP propagates in the medium excited by a strong pump SPP pulse. The dissipated energy of the strong SPP pump heats both electron and lattice subsystems of the sample, and this temperature rise translates into the change in the dielectric constant for a weaker collinear probe plasmon. The main mechanisms of such variations are the intraband and interband transitions in noble-metal substrate (see, e.g., Ref. [2]). The former are well described by a free-electron Drude model where electrons oscillate in response to the pump electric field. The temperature effects enter the Drude model via the increased electron-electron (e-e) and electron-phonon (e-ph) scattering rates thus providing the nonzero imaginary part of the dielectric constant. The interband transitions are more subtle and occur from the lower valence (*d*) band to the higher conduction (*s*) band due to the heating-induced Fermi smearing. It has been well known experimentally [11] that the contribution of the interband transitions cannot be neglected in noble metals at high energies (corresponding to the visible range).

In this paper we show that by combining a well-established two-temperature model (TTM) [12] for the temperature dynamics of the electron and lattice subsystems with the full account of both the intra- and interband transitions we can achieve a significant control of the losses (extinction coefficient) for a probe plasmon in the visible and near-infrared (NIR) region. Moreover, we show that one can even achieve an increased transmission around the green wavelength ($\lambda \sim 500$ nm) by a pump wave working on the same wavelength. Such an effect cannot be explained by the free-electron (Drude) model, and we attribute this effect solely to the interband transition mechanisms.

*stasd@bgu.ac.il

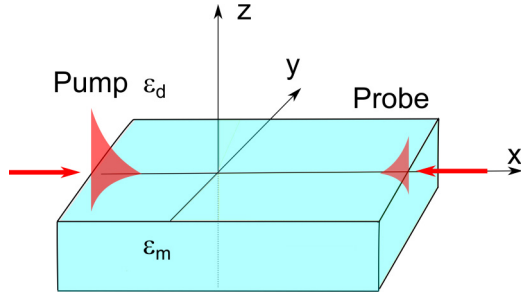


FIG. 1. Problem geometry.

This mechanism of controlling electromagnetic properties of the SPP probe is somewhat reminiscent of the fast-developing area of plasmonic photocatalysis in semiconductors where the absorbed photons are creating active electrons and holes, which can then initiate the reduction and/or oxidation of chemicals. This effect is drastically enhanced by introducing noble-metal nanoparticles; see, e.g., recent reviews [13,14]. While in this paper we are dealing with a different type of medium (bulk noble metals) and different mechanism (temperature), this analogy is still illuminating.

The paper is organized as follows: In Sec. II introduce the main dynamical model (TTM driven by the pump plasmon). In Sec. III solve the model in the quasilinear case when the temperature change induced by the pump is relatively small and compare the results with the full numerical simulations. In Sec. IV we show how this temperature change translates to the transient change in the effective extinction coefficient for the weak probe plasmon (not strong enough to induce additional change in temperature). Finally, in Sec. V we summarize the findings and provide an outlook for further lines of research.

II. PUMP-INDUCED SPATIOTEMPORAL DYNAMICS OF ELECTRONIC AND LATTICE TEMPERATURES

Consider a strong SPP pump pulse propagating along a metal-dielectric interface $z = 0$ with piecewise constant dielectric function $\varepsilon(z) = \varepsilon_d$, $z > 0$; $\varepsilon(z) = \varepsilon_m(z)$, $z < 0$. Assuming the x -traveling mode ($k_y = 0$), the pump field expressions take the form [2]

$$\begin{aligned} \vec{H}_0 &= A(t) (0, 1, 0) e^{i k_x x + \kappa(z) z - i \omega_0 t}, \\ \vec{E}_0 &= \frac{A(t)}{\omega_0 \varepsilon_0 \varepsilon(z)} (-i \kappa(z), 0, -k_x) e^{i k_x x + \kappa(z) z - i \omega_0 t}, \\ \kappa(z) &= -\text{sgn}[z] \sqrt{k_x^2 - k_0^2 \varepsilon(z)}, \quad k_0 = \omega_0/c, \\ k_x &= k_0 \sqrt{\frac{\varepsilon_d \varepsilon_m}{\varepsilon_d + \varepsilon_m}}, \quad \text{Re}(k_x) \geq k_0 \sqrt{\varepsilon_d}. \end{aligned} \quad (1)$$

Here, we assume that the localization length in metal is much less than the width of the metal film so that we are in a bulk geometry and the effects of the substrate can be neglected. The geometry is shown in Fig. 1.

The pump amplitude $A(t)$ is a slowly varying envelope function with the characteristic time scale τ_p . To be specific, we shall assume a Gaussian pulse shape, $A(t) = A_0 \exp(-t^2/2\tau_p^2)$. We shall also assume that the spatial region of interest is rather small and the pulse is long enough so

that one can neglect the dispersion spreading of the pump pulse (although such effects can in principle be taken into account [15]).

The electromagnetic energy dissipated in the bulk of the metal acts as a source of heat diffusion described by a well-established two-temperature model (TTM) for the electron and lattice subsystems [12]:

$$\begin{aligned} C_e(T_e) \frac{\partial T_e}{\partial t} &= \nabla \cdot [K_e(T_e, T_l) \nabla T_e] - G(T_e - T_l) + p_{\text{abs}}, \\ C_l(T_l) \frac{\partial T_l}{\partial t} &= \nabla \cdot [K_l(T_l) \nabla T_l] + G(T_e - T_l). \end{aligned} \quad (2)$$

Here, $C_{e,l}$ and $K_{e,l}$ are the heat capacities and thermal conductivities of the electrons and the lattice, and G is the electron-phonon coupling factor related to the rate of energy exchange between the electrons and the lattice. Note that both heat capacities and thermal conductivities depend explicitly on both temperatures, which makes the TTM model nonlinear.

The energy dissipation caused by the pump field is proportional to the imaginary part of the dielectric permittivity [16]:

$$\begin{aligned} p_{\text{abs}}(x, z, t) &= \varepsilon_0 \varepsilon_m'' \omega |\vec{E}_0(x, z, t)|^2 / 2 \\ &= p_0 e^{-t^2/\tau_p^2} e^{-x/\delta_x} e^{z/\delta_z}, \end{aligned} \quad (3)$$

where

$$\delta_x^{-1} = 2 \text{Im}(k_x), \quad \delta_z^{-1} = 2 \text{Re}(\sqrt{k_x^2 - k_0^2 \varepsilon_m}) \quad (4)$$

are propagation and transverse SPP depths, respectively. For the NIR and larger wavelengths these can be estimated from the Drude theory [2]. If the carrier frequency ω is not too close to the plasma frequency, the imaginary part of the dielectric function ε_m'' is much less than the (negative) real one, and in noble metals one has δ_z of the order of a few tens of nanometers while δ_x is usually a few tens to hundreds of micrometers although it can decrease to as low as a few micrometers in the visible range.

III. LINEAR THEORY

The full TTM (2) is clearly nonlinear and can only be solved exactly using numerical simulations (see the end of this section). However, in order to get some insight into the typical scales and effects, an analytical solution can be sought using a perturbation theory. We shall assume that initially both the film and the dielectric are at the same equilibrium temperature T^{eq} and the deviation of both subsystems from thermal equilibrium resulting from the irradiation is small. Then we can linearize Eqs. (2), namely,

$$\begin{aligned} T_e(\vec{r}, t) &= T^{\text{eq}} + \delta T_e(\vec{r}, t), \quad \delta T_e \ll T^{\text{eq}}, \\ T_l(\vec{r}, t) &= T^{\text{eq}} + \delta T_l(\vec{r}, t), \quad \delta T_l \ll T^{\text{eq}}, \end{aligned} \quad (5a)$$

Moreover, the smallness of the temperature deviation allows us to neglect the spatiotemporal dependence of the heat capacity and thermal conductivity so that

$$C_{e,l} \approx C_{e,l}^{\text{eq}} \gg \Delta C_{e,l}, \quad \delta K_{l,e} \ll K_{e,l} \approx K_{l,e}^{\text{eq}}. \quad (6)$$

TABLE I. Parameters used in the solution of the original (2) and linearized [(7a)–(7c)] TTM.

Parameter	Value	Units	Ref.
C_e^{eq}	2.1×10^4	$\text{J m}^{-3} \text{K}^{-1}$	[17]
C_l^{eq}	2.5×10^6	$\text{J m}^{-3} \text{K}^{-1}$	[17]
G	2.5×10^{16}	$\text{J m}^{-3} \text{K}^{-1} \text{s}^{-1}$	[18]
D_e	0.015	m^2/s	
D_l	2.5×10^{-6}	m^2/s	
Γ_{T_l}	1×10^{10}	s^{-1}	[19]
Γ_{T_e}	1.2×10^{12}	s^{-1}	[19]
λ_{pump}	500	nm	
K_e^{eq}	315	$\text{W m}^{-1} \text{K}^{-1}$	[17]
K_l^{eq}	2.5	$\text{W m}^{-1} \text{K}^{-1}$	[20]
l	20	nm	[2]
δ_z	10	nm	
δ_x	10	μm	
τ_p	$0.1 \div 10$	ps	

Substitution of Eqs. (5a) and (5a) into Eqs. (2) and subsequent linearization leads to the following linear system of equations:

$$\frac{\partial \delta T_e}{\partial t} = D_e \nabla^2 \delta T_e - \Gamma_{T_e} (\delta T_e - \delta T_l) + f(\vec{r}, t), \quad (7a)$$

$$\frac{\partial \delta T_l}{\partial t} = D_l \nabla^2 \delta T_l + \Gamma_{T_l} (\delta T_e - \delta T_l), \quad (7b)$$

$$f(\vec{r}, t) \equiv \frac{P_{\text{abs}}(\vec{r}, t)}{C_e^{\text{eq}}}, \quad (7c)$$

where $\Gamma_{T_{e,l}}$ and $D_{e,l}$ represent the decay rates and diffusion coefficients of the electronic and lattice temperatures, respectively,

$$\Gamma_{T_e} \equiv \frac{G}{C_e^{\text{eq}}}, \quad D_e \equiv \frac{K_e^{\text{eq}}}{C_e^{\text{eq}}}, \quad (8a)$$

$$\Gamma_{T_l} \equiv \frac{G}{C_l}, \quad D_l \equiv \frac{K_l^{\text{eq}}}{C_l}. \quad (8b)$$

Typical values of parameters used in the analytical solution of the linearized TTM [Eqs. (7a)–(7c)] are given in Table I.

The procedure for solving the linearized TTM model was described in Ref. [9]. Here, however, we shall use a simplifying assumption which makes the analysis much easier.

First, as noted previously the longitudinal length of the pump plasmon δ_x is much larger than the transverse one δ_z . As we shall see further in Sec. IV a typical value of δ_x for gold in the visible range is $\delta_x \sim 10 \mu\text{m}$.

Therefore the maximum value of $(D_e t)^{1/2}/\delta_x \sim (D_e/\Gamma_e)^{1/2}/\delta_x \sim 0.01 \ll 1$ (according to Table I), and the inequality is even stronger for the lattice. This means that both electron and lattice diffusion in the longitudinal x direction can be safely neglected and the temperature distributions in this direction follow the slow decay of the source $\sim \exp(-x/\delta_x)$. This allows us to drop the x dependence altogether and consider an essentially one-dimensional spatiotemporal dynamics in the transverse direction (t, z) for the longitudinal distances of a

few micrometers or less. This dependence can be restored by reintroducing the factor $\exp(-x/\delta_x)$.

Next we notice from Table I that both the diffusion coefficient and the decay rate for the lattice are smaller than their electronic counterparts: $D_l \ll D_e$, $\Gamma_{T_l} \ll \Gamma_{T_e}$. This means that the induced change in the lattice temperature is much smaller than that for the electrons, $\delta T_e \gg \delta T_l$. Thus in the first approximation the heating of the electronic subsystem does not depend on the lattice. We can then solve Eq. (7a) assuming $\delta T_l = 0$ and then substitute the found solution into Eq. (7b) as the effective source.

For both temperature disturbances we assume the zero-flux (Neumann) boundary condition at the metal-dielectric interface $z = 0$, and the equations are solved in the semi-infinite region $z < 0$ occupied by the metal.

A. Electronic subsystem

We start from the electronic subsystem (7a), where according to our approximation we neglect the lattice term. This is a damped diffusion equation and its Green's function in the free space can be easily obtained using the standard Fourier method. The result reads

$$\begin{aligned} G(\Delta z; \Delta t) &= \frac{\theta(\Delta t)}{\sqrt{4\pi D_e \Delta t}} \exp[-\Gamma_{T_e} \Delta t] \exp\left[-\frac{\Delta z^2}{4D_e \Delta t}\right] \\ &= G^{(0)}(\Delta z; \Delta t) \exp[-\Gamma_{T_e} \Delta t], \end{aligned} \quad (9)$$

where $\Delta z = z - z'$, $\Delta t = t - t'$, $\theta(t)$ is the Heaviside theta function and $G^{(0)}$ is the undamped Green's function of the free space.

Next, to get the Green's function in the considered semi-infinite geometry with the Neumann boundary condition, one can use the method of images (see, e.g., Ref. [21]):

$$\begin{aligned} G(z, z'; \Delta t) &= (G^{(0)}(z - z'; \Delta t) + G^{(0)}(z + z'; \Delta t)) \\ &\quad \times \exp[-\Gamma_{T_e} \Delta t]. \end{aligned} \quad (10)$$

Physically, the two terms above represent the (damped) free-space contributions from the genuine source z' and its symmetric image $-z'$. Thus the response of the system to the excitation (3) can be written as

$$\begin{aligned} \delta T_e(z, t) &= \int_{-\infty}^t dt' \int_{-\infty}^0 dz' G(z, z'; t - t') \frac{P_0(z', t')}{C_e^{\text{eq}}} \\ &= \int_{-\infty}^t dt' [F(z; t - t') + F(-z; t - t')] \\ &\quad \times e^{-\Gamma_{T_e}(t-t')} e^{-t'^2/\tau_p^2} \\ F(z; \Delta t) &= \frac{P_0}{2C_e^{\text{eq}}} e^{D_e \Delta t / \delta_z^2 + z/\delta_z} \\ &\quad \times \text{erfc}\left[\frac{(D_e \Delta t)^{1/2}}{\delta_z} + \frac{z}{2(D_e \Delta t)^{1/2}}\right], \end{aligned} \quad (11)$$

with $\text{erfc}(x)$ being the complementary error function. In general, the time integrals cannot be evaluated analytically, but the treatment is simplified in two limiting cases: ultrafast (femtosecond) pulses and long (> 1 ps) pulses.

1. Ultrafast pulse

In the ultrafast-pulse case, $\Gamma_{Te}\tau_p \ll 1$, which according to Table I corresponds to femtosecond pulses. Thus one can substitute the pulse with the impulse response: $\exp(-t'^2/\tau_p^2) \approx \sqrt{\pi} \tau_p \delta(t')$. Assuming that the observation time is not too small, $t \gtrsim \tau_p$, one has

$$\begin{aligned} \delta T_e(z, t) &= \sqrt{\pi} \tau_p [F(z; t) + F(-z; t)] e^{-\Gamma_{Te} t}, \\ \Gamma_{Te} \tau_p &\ll 1 \text{ and } t \gtrsim \tau_p. \end{aligned} \quad (12)$$

The above expression can be further simplified if we notice that the minimum value of the parameter $(D_e t)^{1/2}/\delta_z \sim (D_e \tau_p)/\delta_z \sim 4$ for a 100-fs pulse. Therefore the argument of the complementary error function is large almost everywhere apart from the vicinity of the resonance time line $z_*(t) = -2(D_e t)/\delta_z$. This line naturally splits the metal region into a near zone ($|z| \ll z_*$) and a far zone ($|z| \gg z_*$). In both zones we can therefore use a large-argument expansion of the complementary error function:

$$\operatorname{erfc}(x) \approx 2 \theta[-x] + \frac{e^{-x^2}}{\sqrt{\pi x}}, \quad |x| \gg 1.$$

Then after some algebra we obtain the final result up to the main terms:

$$\begin{aligned} \delta T_e(z, t) &= \frac{p_0 \tau_p}{C_e^{\text{eq}}} e^{-\Gamma_{Te} t} \begin{cases} \frac{\delta_z}{\sqrt{D_e t}} e^{-z^2/4D_e t}, & |z| \ll z_*(t) \\ e^{z/\delta_z}, & |z| \gg z_*(t) \end{cases} \\ \text{for } \Gamma_{Te} \tau_p &\ll 1 \text{ and } t \gtrsim \tau_p. \end{aligned} \quad (13)$$

Therefore one can see that the temperature in metal experiences damped diffusion in the internal direction z in the near zone followed by exponential decay with the same exponent δ_z in the far zone. Uniform temporal decay is observed throughout (with the exponent Γ_{Te}).

The typical value of the transition boundary is given by $z(\tau_p) = 2(D_e \tau_p)/\delta_z \sim 300$ nm (for a 100-fs pulse), which is much deeper than the plasmon decay δ_z .

2. Long pulses

In the long-pulse case, one has $\Gamma_{Te} \tau_p \gg 1$, which according to Table I corresponds to pulses of duration of a few tens of picoseconds. Thus we can approximate $\exp(-t'^2/\tau_p^2)$ with its value at $t' = t$, and the temporal dependence of the temperature disturbance follows exactly the pulse shape. Consequently, the value of the integral in (12) is time independent, and the main contribution comes from the region $t - t' \sim \Gamma_{Te}^{-1}$.

We are thus left with an integral:

$$\begin{aligned} \delta T_e(z, t) &= \frac{p_0}{2C_e^{\text{eq}}} e^{-t^2/\tau_p^2} [f(z) + f(-z)], \\ f(z) &= \int_0^\infty e^{D_e \Delta t / \delta_z^2 + z/\delta_z} \\ &\quad \times \operatorname{erfc} \left[\frac{(D_e \Delta t)^{1/2}}{\delta_z} + \frac{z}{2(D_e \Delta t)^{1/2}} \right] e^{-\Gamma_{Te} \Delta t} d\Delta t. \end{aligned}$$

Introducing the change of variables $\tau = (D_e \Delta t / \delta_z^2)^{1/2}$, $\zeta = z/\delta_z$, $\delta'_z = (D_e / \Gamma_{Te})^{1/2} = \xi \delta_z$, we can write

$$f(\zeta) = \frac{2\delta_z^2}{D_e} \int_0^\infty e^{\tau^2 + \zeta} \operatorname{erfc} \left[\tau + \frac{\zeta}{2\tau} \right] e^{-\tau^2/\xi^2} \tau d\tau.$$

Remarkably, this integral can be evaluated in the closed form. It is easy to check that it satisfies the following ordinary differential equation (ODE):

$$\begin{aligned} \frac{df}{d\zeta} &= f(\zeta) - \frac{2\delta_z^2}{\sqrt{\pi} D_e} \int_0^\infty e^{-\zeta^2/4\tau^2 - \tau^2/\xi^2} d\tau \\ &= f(\zeta) - \frac{\delta_z^2}{D_e} \xi e^{-|\zeta|/\xi}, \end{aligned}$$

where in the second line we have used a table integral (Ref. [22], Eq. 3.325). This equation can be easily solved using the initial condition $f(0) = (\delta_z^2/D_e)\xi^2/(1+\xi)$ (which can be obtained by integrating by parts) obtaining

$$f(\zeta) = \frac{\delta_z^2}{D_e} \xi^2 \left[\frac{e^\zeta}{\xi+1} + \frac{e^{-|\zeta|/\xi} - e^\zeta}{\xi + \operatorname{sgn}(\zeta)} \right].$$

Taking the symmetric combination of the above, the final answer for the electron temperature reads

$$\delta T_e(z, t) = \frac{p_0}{G} e^{-t^2/\tau_p^2} \frac{e^{z/\delta_z} \xi - e^{-z/\delta_z}}{\xi^2 - 1}. \quad (14)$$

One can easily verify that the above solution indeed has a vanishing flux in the z direction at the interface.

Note that for the slow pulse the nature of the electron temperature distribution inside the metal changes. Instead of the diffusive spread (13), one now has an exponential decay with the two scales, δ_z and $\delta'_z = \xi \delta_z$. Typical values of parameter ξ according to Eq. (4) and Table I are $\xi \approx 10$. So there is a strong component decaying at the enlarged effective skin depth $\delta'_z \sim 100$ nm and a weaker component decaying at the original skin depth $\delta_z = 10$ nm whose role is to provide the vanishing flux at the metal-dielectric interface.

From Eq. (14), one can approximate the peak value of the electron temperature disturbance occurring at the origin at the center of the temporal pulse, $t = 0$:

$$\delta T_{e,\max} = \frac{p_0}{G(\xi+1)}. \quad (15)$$

Thus for the input power density $p_0 = 3$ MJ/(ps m³) the maximum electron temperature change is estimated as $\delta T_{e,\max} = 9.7$ K.

B. Lattice subsystem

Next, for the lattice temperature, one notices that the equation for the lattice dynamics (7b) has the same form as that for the electrons only with the replacement of the electron decay rates and diffusion with their lattice counterparts $\Gamma_{Te} \rightarrow \Gamma_{Tl}$, $D_e \rightarrow D_l$ and the role of the source is now being played by the electron temperature perturbation $f \rightarrow \Gamma_{Tl} \Delta T_e$. We can therefore reuse most of the results from the previous section. We concentrate here on the case of a ‘‘slow’’ pulse $\Gamma_{Te} \tau_p \gg 1$ as the most interesting one.

The important difference in the lattice dynamics is that it is very slow (inertial) compared with its electronic counterpart.

Thus, for example, a pulse of duration 1–10 ps which can be considered slow with respect to the electron subsystem will have the typical values of $\Gamma_{T_e} \tau_p \sim 0.01\text{--}0.1$, i.e., the electron temperature variation acting as a source for the lattice can be considered fast. Therefore we can reuse most of the arguments from Sec. III A 1. Moreover, according to the solution (14) the spatiotemporal dependence of the electron temperature in the regime of large ξ which is considered here mimics that of the original perturbation up to the prefactor and the replacement $\delta_z \rightarrow \delta'_z \gg \delta_z$.

Thus, making use of the ready expressions (11) and (12), we immediately obtain

$$\begin{aligned} \delta T_l(z, t) &= \sqrt{\pi} \tau_p [\tilde{F}(z; t) + \tilde{F}(-z; t)] e^{-\Gamma_{T_l} t}, \quad t \gtrsim \tau_p, \\ \tilde{F}(z; t) &= \frac{p_0 \Gamma_{T_l}}{2 C_e^{\text{eq}} \xi \Gamma_{T_e}} e^{D_l t / \delta_z^2 + z / \delta'_z} \\ &\quad \times \operatorname{erfc} \left[\frac{(D_l t)^{1/2}}{\delta'_z} + \frac{z}{2(D_l t)^{1/2}} \right]. \end{aligned} \quad (16)$$

However, in the z direction, one has $(D_l t)^{1/2} / \delta'_z \sim (D_l / \Gamma_{T_l})^{1/2} / \delta'_z \sim 0.14$, i.e., also small. This means that unlike the case of an electron subsystem reacting to a fast excitation the lattice diffusion constant is simply too small to diffuse the source on the relevant time scales.

Moreover, using the identity $\operatorname{erfc}(-x) = 2 - \operatorname{erfc}(x)$, it is easy to see that

$$\begin{aligned} e^{z/\delta'_z} \operatorname{erfc} \left[\frac{z}{2(D_e \Delta t)^{1/2}} \right] + e^{-z/\delta'_z} \operatorname{erfc} \left[-\frac{z}{2(D_e \Delta t)^{1/2}} \right] \\ = -2e^{z/\delta'_z} + 2 \sinh(z/\delta'_z) \operatorname{erfc} \left[-\frac{z}{2(D_e \Delta t)^{1/2}} \right]. \end{aligned} \quad (17)$$

So the answer can be rewritten as

$$\begin{aligned} \delta T_l(z, t) &= \frac{\sqrt{\pi} \Gamma_{T_l} \tau_p p_0}{G \xi} \left(e^{z/\delta'_z} - 2 \sinh(z/\delta'_z) \right) \\ &\quad \times \operatorname{erfc} \left[-\frac{z}{2(D_l t)^{1/2}} \right] e^{-\Gamma_{T_l} t}, \quad t \gtrsim \tau_p. \end{aligned} \quad (18)$$

During the lifetime of the lattice disturbance $t_l \sim \Gamma_{T_l}^{-1} \sim 100$ ps the second term (representing the diffusion effects) can be neglected, and the electron and lattice temperature disturbances at each point are proportional to the time-dependent proportionality factor given by

$$\frac{\delta T_l(z, t)}{\delta T_e(z, t)} = (\Gamma_{T_l} \tau_p)^{-1} \frac{1}{\sqrt{\pi}} e^{-t^2/\tau_p^2 + \Gamma_{T_l} t}, \quad t \gtrsim \tau_p. \quad (19)$$

Thus during the duration of the plasmon pump $|t| \sim \tau_p$ the electron-associated temperature disturbance dominates with $\delta T_e / \delta T_l \sim (\Gamma_{T_l} \tau_p)^{-1} \gg 1$; after the initial pulse duration the electron component dies down, and there exists only a small but persistent change in the lattice temperature up to the times t_l .

Finally, in order to verify the validity of the linear theory considered above, we have performed full numerical simulations of system (2) using well-known temperature dependencies of heat capacities and thermal conductivities of the electron and lattice subsystems (see, e.g., Ref. [9]). Equations (2) represent a system of coupled nonlinear partial

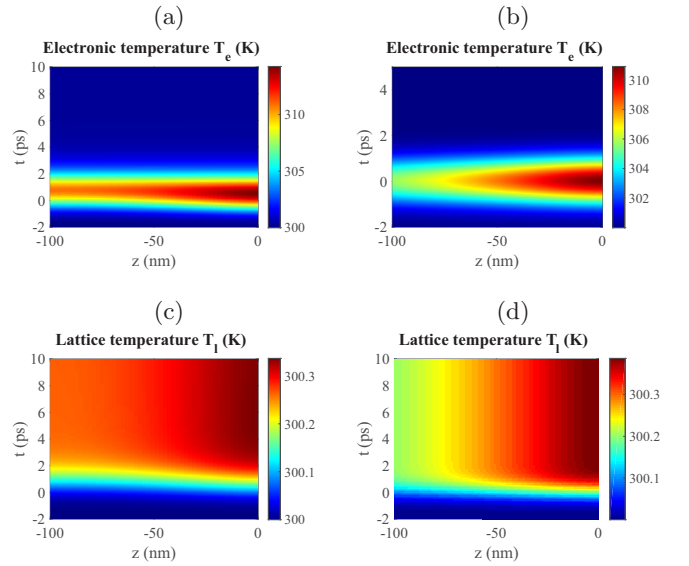


FIG. 2. The spatiotemporal evolution of the induced temperature distribution when $p_0 = 3$ MJ/(ps m³) and $\tau_p = 1$ ps. (a) and (b) Electron temperature T_e and (c) and (d) lattice temperature T_l . (a) and (c) Full numerics and (b) and (d) linear theory.

differential equations (PDEs) that can be solved using standard numerical methods (we used a standard MATLAB PDE mesh-grid solver). The analytical and numerical results for T_e and T_l are represented in Figs. 2 and 3.

One can observe a reasonably good quantitative agreement between theory and numerics. Moreover, the qualitative spatiotemporal shape of the temperature disturbance is preserved even for much higher energy density where the temperature variation for the electron subsystem is not small and the perturbative analysis above is technically inapplicable; see Fig. 4.

IV. TEMPERATURE-INDUCED TRANSMISSIVITY CHANGES

In this section we shall study how the temperature variations studied above and induced by a strong pump plasmon translate into the change in the dielectric properties of the medium for the weak coplanar probe plasmon.

Most of the results cited in the literature regarding the temperature effects on the electromagnetic properties of noble metals assume a simple Drude model for the dielectric

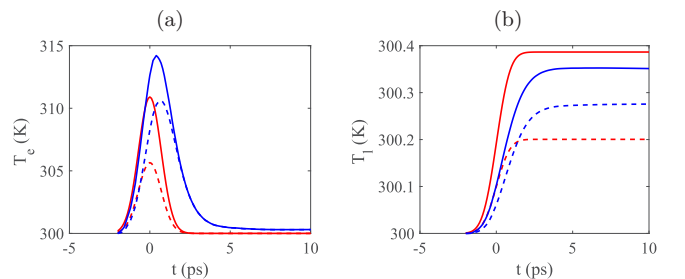


FIG. 3. Analytical (red) and numerical (blue) temporal dependence of the electron T_e (a) and lattice T_l (b) temperatures at $z = 0$ (solid) and $z = 100$ nm (dashed) curves.

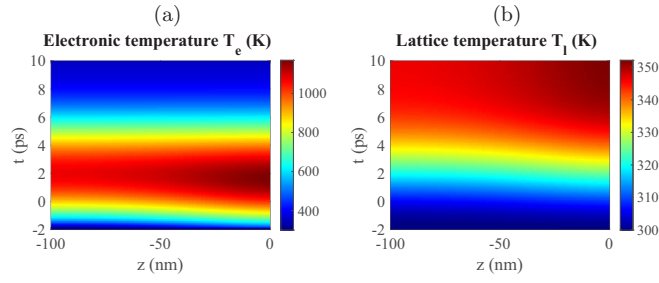


FIG. 4. Spatiotemporal variation of (a) T_e and (b) T_l assuming that the incident energy density is $p_0 = 0.2 \text{ GJ}/(\text{ps m}^3)$ and $\tau_p = 3 \text{ ps}$.

permittivity [2]:

$$\varepsilon_m = 1 - \frac{\omega_p^2}{\omega(\omega + i\gamma)}, \quad (20)$$

where ω_p is the plasma frequency and γ is the electron scattering rate. This model describes only intraband transitions, and the electron and lattice heating as described in the previous section is translated into the monotonic increase of the scattering rate γ . An important consequence of this is that the imaginary part of the permittivity is given by

$$\varepsilon_m'' = \text{Im } \varepsilon_m = \frac{\omega_p^2 \gamma}{\omega(\omega^2 + \gamma^2)}$$

and it grows with the scattering rate (and hence the temperature) up to $\gamma = \omega$. However, in the near-infrared and visible region the Drude model is not sufficient to explain empirical measurements because of two interband absorption peaks at $\lambda = 500$ and 730 nm [23,24]. In this paper, we show that if the latter are taken into account, the variability of the induced losses is much higher, and one can even observe a pump-induced increase in the probe propagation in the visible part of the spectrum.

To account for the effect of interband transitions on optical properties of Au, we use the model developed in Refs. [23–28]. In Fig. 5, we compare the experimental data of Johnson and Christy [11] with the theoretical model of Stoll *et al.* [25] assuming that the metal is at room temperature. We can see that the model almost perfectly describes the data in the visible region.

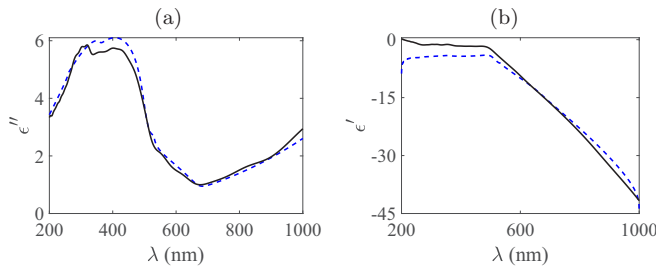


FIG. 5. Wavelength dependence of the dielectric function of Au assuming that $T_e = T_l = 300 \text{ K}$: (a) imaginary part and (b) real part. The blue dashed curve represents the data obtained by the use of the model of Stoll *et al.* [25], while the black solid curve represents the experimental data of Ref. [11].

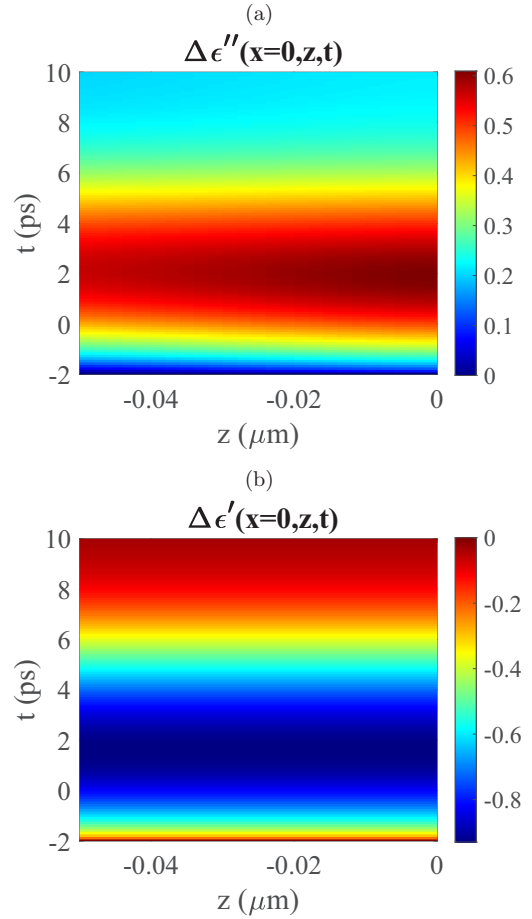


FIG. 6. Variation of the imaginary (a) and real (b) parts of dielectric function of Au assuming that $p_0 = 0.2 \text{ GJ}/(\text{ps m}^3)$, $\tau_p = 3 \text{ ps}$, and $\lambda = 500 \text{ nm}$.

The above comparison between the theoretical calculation of the real and imaginary parts of the dielectric constant and the experimental data is made to validate the assumption that the theoretical model can simulate the experimental data quite well. Thus it can be used for different temperature values. With this in mind, using the TTM (2), we calculate the temperature variation induced by the pump which leads to variation of the inter- and intraband terms of the imaginary and real parts of the dielectric function as felt by a weak probe. It is important that throughout this section we are not relying on the results of Sec. III or the linearized model but rather perform full numerical simulations.

These results are presented in Fig. 6, where both intra- and interband transitions are taken into account. We only plot the relative change in the dielectric constant $\Delta\varepsilon = \varepsilon - \varepsilon_{\text{eq}}$, where ε_{eq} is the equilibrium value of the dielectric function in metal at $T = 300 \text{ K}$. One can clearly see the transient nature of the induced variation of the dielectric constant following the transient nature of the temperature variation as correctly predicted by the linear theory of Sec. III.

After the passing of the pulse excitation the change in the real part of the dielectric constant is washed out, but the change in the imaginary part persists up to the times of the lattice cooling t_p and retains a virtually uniform spatial profile corresponding to $\Delta\varepsilon''_{\text{max}} \approx 0.25$. Therefore in the time interval

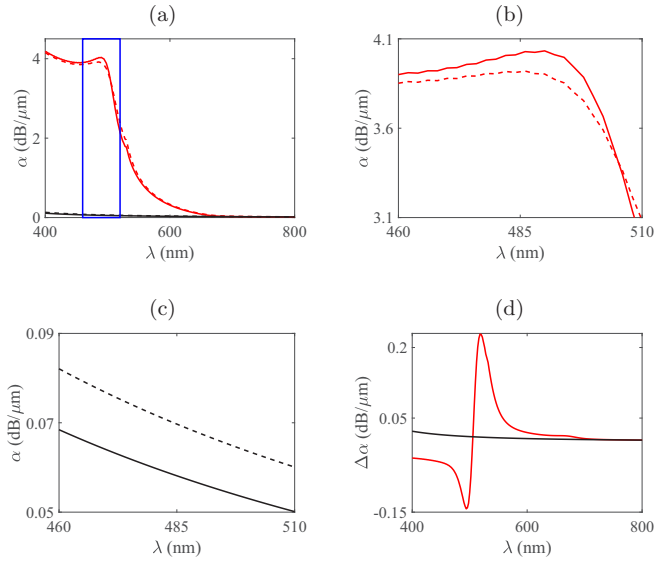


FIG. 7. Spectral dependence of absorption coefficient α (dB/ μm). The solid curves represent the pretransit values ($t = 0$ ps), while the dashed curves are the post-transit ones ($t = 10$ ps). (a) Comparison between Drude model (black) and the full model (red) for Au assuming that $p_0 = 0.2$ GJ/(ps m³), $\tau_p = 3$ ps. (b) Blown-up region [blue rectangle in (a)] which shows the region of increased propagation length for the full model. (c) Same as (b), but for the Drude model. (d) Comparison of the relative change in the absorption coefficient $\Delta\alpha = \alpha(t = 10 \text{ ps}) - \alpha(t = 0 \text{ ps})$ between the Drude model (black solid curve) and the full model (red solid curve).

after the pump transient and up to lattice cooling, i.e., $3 \text{ ps} \leq t \leq 100 \text{ ps}$, the medium remains uniform, and one can use the expressions (1) for the probe plasmon but with the changed dielectric constant of metal.

In particular, according to the Beer-Lambert law the intensity of the probe plasmon decays exponentially with the propagation distance [2]:

$$I_{pr}(x) = I_0 e^{-\alpha x}, \quad \alpha = 2 \text{Im}[k'_x],$$

$$k'_x = k_0 \sqrt{\frac{\varepsilon_d (\varepsilon_m + i\Delta\varepsilon'')}{\varepsilon_d + \varepsilon_m + i\Delta\varepsilon''}}. \quad (21)$$

In the equation above, the absorption coefficient is defined in the asymptotic regions prior to and after the transient of the pump, and it is interesting to compare the two in the visible region where the losses are generally high. In the above equation the correction to the real part of the dielectric function due to the pump contributes only to the higher-order terms in the extinction ratio and therefore can be neglected. It is also interesting to compare these results with the Drude model (20), which, as stated earlier, takes into account only intraband transitions. These results are presented in Fig. 7.

The first observation one makes from Fig. 7(a) is that the Drude model severely underestimates losses in the visible region of the spectrum. The difference disappears at the NIR boundary, where intraband transitions described by the Drude model dominate. More interesting is the difference between pre- and post-transit absorption coefficients. Figure 7(b) shows the enlarged region roughly corresponding to the yellow

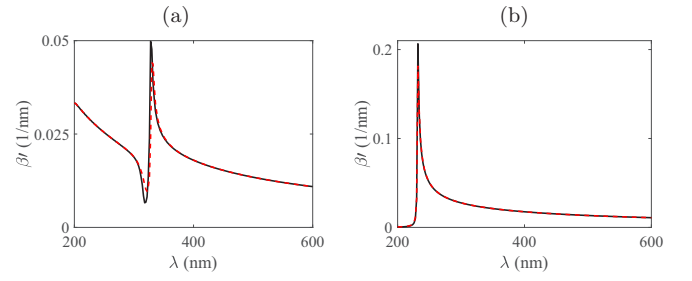


FIG. 8. Spectral dependence of the propagation constant $\beta = \text{Re}[k'_x]$ (nm^{-1}). The solid curves represent the pretransit values ($t = 0$ ps), while the dashed curves are the post-transit ones ($t = 10$ ps). The results are shown for the full model (a) and Drude model (b) for Au assuming that $p_0 = 0.2$ GJ/(ps m³), $\tau_p = 3$ ps.

low wavelength. One can see that in this region the post-transit value is less than the pretransit one, i.e., the pump wave leads to decreased absorption for the probe wave. This is an attribute of the interband transition absent in the Drude model [as attested by Fig. 7(c)]. Moreover, the spectral region where this decreased absorption occurs is relatively narrow, as seen in both Figs. 7(b) and 7(d). Note that the difference between pre- and post-transit propagation distances shown in Fig. 8 is much less pronounced.

How large is this effect in real terms? In our simulations for the waveguide length equal to the typical longitudinal length of an SPP $L \sim \delta_x^{-1} \sim 10 \mu\text{m}$ and for the maximum decrease in the imaginary part of the refractive index $\Delta\varepsilon'' = -0.3$ the increase in the transmittance is constituted by

$$\Delta T = \exp(2\text{Im}[k_x - k'_x]L) \approx 3 \text{ dB}, \quad (22)$$

where k_x is the longitudinal wave vector of the probe prior to the transit of the pump. Thus one can conclude that the induced transmittance gain is quite tangible.

V. CONCLUSION

We have demonstrated that one can strongly control the absorption of the SPP in the visible and NIR region in the pump-probe configuration via temperature-induced changes in the intraband transition in noble metals. A large pump pulse propagating at the metal-dielectric interface heats both electron and lattice subsystems, and the latter leads to large variation of the extinction coefficient for a visible-NIR weak probe plasmon due to the interband transitions in metal. Around the wavelength $\lambda \sim 500 \text{ nm}$ this change can even be negative, i.e., the propagation length can be increased for the probe after the transient of the pump. We estimate that for gold, one can increase the transmission coefficient for the probe by $\sim 3 \text{ dB}$ during a time window of up to 100 ps, which significantly exceeds the few-picosecond duration of the pump pulse. We believe that these findings can help facilitate the development of novel ultrafast plasmonic switches and optoelectronic gates.

Some future avenues of research regarding this problem may include full-wave simulations with wide-band sources in Kretschmann's or Otto's configurations [4,29,30] as well as the study of the edge effects at the probe insertion point [31,32].

- [1] A. Zayats, I. Smolyaninov, and A. Maradudin, Nano-optics of surface plasmon polaritons, *Phys. Rep.* **408**, 131 (2005).
- [2] S. Maier, *Plasmonics: Fundamentals and Applications*, 2nd ed. (Springer-Science, Bath, UK, 2007).
- [3] S. Pillai, F. J. Beck, K. R. Catchpole, Z. Ouyang, and M. A. Green, The effect of dielectric spacer thickness on surface plasmon enhanced solar cells for front and rear side depositions, *J. Appl. Phys.* **109**, 073105 (2011).
- [4] L. Lu, Z. Jiang, Y. Hu, H. Zhou, G. Liu, Y. Chen, Y. Luo, and Z. Chen, A portable optical fiber SPR temperature sensor based on a smart-phone, *Opt. Express* **27**, 25420 (2019).
- [5] S. Darmanyan and A. Zayats, Light tunneling via resonant surface plasmon polariton states and the enhanced transmission of periodically nanostructured metal films: An analytical study, *Phys. Rev. B* **67**, 035424 (2003).
- [6] L. Feng, M. Lu, V. Lomakin, and Y. Fainman, Plasmonic photonic crystal with a complete band gap for surface plasmon polariton waves, *Appl. Phys. Lett.* **93**, 231105 (2008).
- [7] A. Cebrecos, R. Pico, V. Romero-Garcia, A. Yasser, L. Maigyte, R. Herrero, M. Botey, V. J. Sanchez-Morcillo, and K. Staliunas, Enhanced transmission band in periodic media with loss modulation, *Appl. Phys. Lett.* **105**, 204104 (2014).
- [8] A. J. Chaves and N. Peres, Propagation of surface plasmons on plasmonic Bragg gratings, *J. Appl. Phys.* **125**, 243106 (2019).
- [9] M. Spector and S. Derevyanko, Transient temperature induced plasmonic crystal, *Phys. Rev. B* **102**, 174308 (2020).
- [10] Y. Sivan and M. Spector, Ultrafast dynamics of optically-induced heat gratings in metals, *ACS Photon.* **7**, 1271 (2020).
- [11] P. Johnson and R. Christy, Optical constants of noble metals, *Phys. Rev. B* **6**, 4370 (1972).
- [12] S. Anisimov, B. Kapeilovich, and T. Perelman, Electron emission from metal surfaces exposed to ultrashort laser pulses, *Sov. Phys. JETP* **39**, 375 (1974).
- [13] X. Zhang, Y. L. Chen, R. Liu, and D. P. Tsai, Plasmonic photocatalysis, *Rep. Prog. Phys.* **76**, 046401 (2013).
- [14] A. Kumar, P. Choudhary, A. Kumar, P. Camargo, and V. Krishnan, Recent advances in plasmonic photocatalysis based on TiO₂ and noble metal nanoparticles for energy conversion, environmental remediation, and organic synthesis, *Small* **18**, 2101638 (2022).
- [15] Z. L. Sámson, P. Horak, K. MacDonald, and N. Zheludev, Femtosecond surface plasmon pulse propagation, *Opt. Lett.* **36**, 250 (2011).
- [16] E. Lifshitz and L. Pitaevskii, *Electrodynamics of Continuous Media*, 5th ed. (Fizmatlit, Moscow, 2001).
- [17] N. W. Ashcroft and N. D. Mermin, *Solid State Physics* (Saunders College, Philadelphia, 1976).
- [18] P. Allen, Theory of Thermal Relaxation of Electrons in Metals, *Phys. Rev. Lett.* **59**, 1460 (1987).
- [19] C. Sun, F. Vallee, L. Acioli, E. Ippen, and J. G. Fujimoto, Femtosecond tunable measurement of electron thermalization in gold, *Phys. Rev. B* **48**, 12365 (1993).
- [20] Y. Wang, Z. Lu, and X. Ruan, First principles calculation of lattice thermal conductivity of metals considering phonon-phonon and phonon-electron scattering, *J. Appl. Phys.* **119**, 225109 (2016).
- [21] E. Akkermans and G. Montambaux, *Mesoscopic Physics of Electrons and Photons* (Cambridge University Press, Cambridge, 2007).
- [22] I. S. Gradshteyn and I. Ryzhik, *Table of Integrals, Series, and Products*, 5th ed. (Academic Press, San Diego, CA, 1996).
- [23] M. Guerissi, R. Rosei, and P. Winsemius, Splitting of the interband absorption edge in Au, *Phys. Rev. B* **12**, 557 (1975).
- [24] M. Spector, Ultrafast dynamics of charge carriers in laser heated metals, Ph.D. thesis, Ben Gurion University of the Negev, 2020.
- [25] T. Stoll, P. Maioli, A. Crut, N. D. Fatti, C. Voisin, and F. Vallee, Advances in femto-nano-optics: ultrafast nonlinearity of metal nanoparticles, *Eur. Phys. J. B* **87**, 260 (2014).
- [26] R. Rosei, Temperature modulation of the optical transitions involving the Fermi surface in Ag: Theory, *Phys. Rev. B* **10**, 474 (1974).
- [27] R. Rosei, Temperature modulation of the optical transitions involving the Fermi surface in Ag: Experiment, *Phys. Rev. B* **10**, 484 (1974).
- [28] R. Rosei, F. Antonangeli, and U. Grassano, d bands position and width in gold from very low temperature thermomodulation measurements, *Surf. Sci.* **37**, 689 (1973).
- [29] H. Lv, K. Zhang, X. Ma, W. Zhong, Y. Wang, and X. Gao, Optimum design of the surface plasmon resonance sensor based on polymethyl methacrylate fiber, *Phys. Open* **6**, 100054 (2021).
- [30] I. Yaremchuk, V. Fitio, H. Petrovska, and Y. Bobitski, The temperature impact on the characteristics of the surface plasmon resonance sensors element, *Optik* **192**, 162969 (2019).
- [31] C. A. Valagiannopoulos, On smoothening the singular field developed in the vicinity of metallic edges, *Int. J. Appl. Electromagn. Mech.* **31**, 67 (2009).
- [32] C. A. Valagiannopoulos, High selectivity and controllability of a parallel-plate component with a filled rectangular ridge, *PIER* **119**, 497 (2011).